Simulation of Gas Production from Multilayered Hydrate Bearing Media with Fully Coupled Flow, Thermal, Chemical, and Geomechanical Processes using TOUGH+Millstone: Part 1: Numerical Modeling of Hydrates

George J. Moridis · Alejandro F. Queiruga · Matthew T. Reagan

the date of receipt and acceptance should be inserted later

Abstract TOUGH+Millstone has been developed for the analysis of coupled flow, thermal and geomechanical processes associated with the formation and/or dissociation of CH4-hydrates in geological media. It is composed of two constituent codes: (a) a significantly enhanced version of the TOUGH+HYDRATE simulator, v2.0, that accounts for all known flow, physical, thermodynamic and chemical processes associated with the behavior of hydrate-bearing systems undergoing changes and includes the most recent advances in the description of the system properties, coupled seamlessly with (b) Millstone v1.0, a new code that addresses the conceptual, computational and mathematical shortcomings of earlier codes used to describe the geomechanical response of these systems. The capabilities of TOUGH+Millstone are demonstrated in the simulation and analysis of the system flow, thermal and geomechanical behavior during gas production from a realistic complex offshore hydrate deposit.

In the first paper of this series, we discuss the physics underlying the T+H hydrate simulator, the constitutive relationships describing the physical, chemical (equilibrium and kinetic) and thermal processes, the states of the CH_4+H_2O system and the sources of critically important data, as well as the mathematical approaches used for the development of the of mass and energy balance equations and their solution. Additionally, we provide verification examples of the hydrate code against numerical results from the simulation of laboratory and field experiments.

Keywords Methane hydrates · Reservoir Simulation · Geomechanics · Coupled processes

1 Introduction

Gas hydrates are solid crystalline compounds of water and gaseous substances described by the formula $G \cdot N_H H_2O$, in which the molecules of gas G (guests) occupy voids within the lattices of

G. Moridis
Petroleum Engineering Department, Texas A&M University, United States
Energy Geosciences Division, Lawrence Berkeley National Laboratory, California, United States
E-mail: moridis@tamu.edu; GJMoridis@lbl.gov

A. Queiruga
Energy Geosciences Division, Lawrence Berkeley National Laboratory, California, United States
E-mail: afqueiruga@lbl.gov

M. Reagan
Energy Geosciences Division, Lawrence Berkeley National Laboratory, California, United States
E-mail: mtreagan@lbl.gov

ice-like crystal structures with N_H (the hydration number) water molecules per gas molecule. The formation and dissociation of hydrates is described by the general equation:

$$G + N_H\, H_2O = G\bullet N_H\, H_2O + \Delta H^0 \tag{1}$$

where ΔH_0 is the enthalpy of formation/dissociation. Note that hydrate formation is an exothermic process.

Gas hydrate (GH) deposits occur in two different geographic settings where the necessary conditions of low temperature T and high pressure P exist for their formation and stability: in the Arctic (typically in association with permafrost) and in deep ocean sediments (Kvenvolden, 1988). The majority of naturally-occurring hydrocarbon GH contain primarily CH_4. Pure CH_4-hydrates contain a factor of 164 more concentrated methane compared to standard P and T conditions (STP). Natural CH_4-hydrates crystallize mostly in the structure I form, which has a hydration number N_H ranging from 5.77 to 7.4, with and average of $N_H = 6$ and complete hydration at $N_H = 5.75$ (Sloan and Koh, 2008). Natural GH can also contain other hydrocarbons (alkanes C_nH_{2n+2}, n = 2 to 4) and trace amounts of other gases (mainly CO_2, H_2S or N_2).

This series presents a comprehensive description of the physical equations, material relations, and numerical algorithms required to simulate oceanic hydrate reservoirs with characteristics observed in real formumations. Due to the scope of this problem, the presentation is seperated into three parts. The first two parts each detail the formulation and algorithms of the two computational simulators developed for these problems and are meant to serve as an exhaustive guide to replicate the analysis and inform future algorithmic developments. The third part of this describes a representative system of methane production from a realistic oceanic hydrate system.

In this paper we describe TOUGH+HYDRATE v2.0 (T+H), the first of the two constituent codes of the TOUGH+Millstone simulator, developed for the analysis of coupled flow, thermal and geomechanical processes associated with the formation and dissociation of hydrates in geological media. The TOUGH+HYDRATE simulator accounts for all known flow, physical, thermodynamic and chemical processes associated with the behavior of hydrate-bearing systems. The second constituent code is the Millstone v1.0 geomechanical simulator, which is the subject of the second paper of this series. In the absence of strong geomechanical effects, TOUGH+HYDRATE can be used as a stand-alone code, uncoupled from Millstone.

2 Background

The TOUGH+HYDRATE code (T+H) (Moridis et al., 2008) has been continually developed at Lawrence Berkeley National Laboratory (LBNL) to model non-isothermal CH_4 release, phase behavior and flow under conditions of both naturally-occuring and laborary-made CH_4-hydrate deposits by solving the coupled equations of fluid flow and heat balance. T+H is a successor to earlier simulators from LBNL first released in 1998 (Moridis et al., 1998; Moridis, 2003; Moridis and Collett, 2004; Moridis et al., 2004, 2005) for application to large-scale simulations of hydrate behavior.

The current version (V2.0) is the third update of the 2008 T+H code (Moridis et al., 2008). It models all known processes involved in natural CH_4-hydrates in complex geologic media using either an equilibrium or a kinetic model (Kim et al., 1987; Clarke and Bishnoi, 2001; Moridis et al., 2008). It includes fluid and heat transport, the thermophysical properties of reservoir fluids, thermodynamic changes and phase behavior, and the non-isothermal chemical reaction of CH_4-hydrate formation and dissociation. T+H is a fully implicit compositional simulator that accounts for heat and up to four mass components (i.e., H_2O, CH_4, CH_4-hydrate, and water-soluble inhibitors such as salts or alcohols) that are partitioned among four possible phases: gas, aqueous liquid, ice, and hydrate. The T+H code can describe all 15 possible thermodynamic states of the CH_4+H_2O system and any combination of the three main dissociation methods: depressurization, thermal

stimulation, and the effect of inhibitors. As will be demonstrated in this series, T+H was designed to handle the phase changes, state transitions, and strong nonlinearities that are typical of hydrate dissociation problems.

This paper presents significant features have been added to this latest version to enable simmulation of observed hydrate reservoir characteristics, in the scope of a complete description of the entire physical formulation.

Hydrate reservoirs are often characterized by very low permeability, neccessitating consideration of Klinkenberg diffusion and Knusden flow. Convserly, in regions near the well, the gas-dominated regions exhibit extremely fast flow requiring Forcheimer flow. Very long term studies to which T+H has been applied exhibit diffusion-dominated transport of methane through the aqueous phase.

Numerous architerctural improvements have been made to the code, described 5

The coupling to the Millstone geomechanical code is another significant alteration to the T+H code itself, which will be described in Part 2. The periodically updated manual to T+H (Moridis and Pruess, 2014) contains more in-depth descriptions of every capability that was not required for the hydrate reservoir simulation presented in Part 3. T+H V2.0 incorporates a series of important new capabilities. These include:

- Consideration of Klinkenberg (1941) flow (non-Darcian, gas slippage effects) for hydrate-bearing media with low effective permebility (e.g., usually associated with medium to high hydrate saturations)
- Knusden flow (non-Darcian) for hydrate-bearing media with extremely effective permebility (e.g., usually associated with high to very high hydrate saturations), and ability to seamlessly move from the Knudsen flow regime to the Klinkenberg regime
- Forchheimer (1901) flow (non-Darcian) for high-velocity flow regimes in the vicinity of wells in high-permeability media
- Multi-component diffusion capabilities, which are important in long-term (geologic time) simulations focusing on hydrate formation (especially associated with super-saturation in oceanic environments)
- Advanced viscosity computation options, including the friction theory of Quinones et al. (2000)
- New option for the estimation of the departure enthalpy equation using the Lee-Kessler (1975) method for mixtures of polar and non-polar materials (water and CH_4)
- Expansion of the phase diagram and properties of H_2O by including Region III (IAPWS, 2007; 2009) describing properties in the vicinity of the critical point, thus making possible consideration of thermal dissociation of hydrates at high pressures and temperatures
- Addition of an option for the ab initio computation of hydrate properties using the Ballard (2002) method
- Addition of the LIS package (Nishida, 2010) for significantly faster solution of the matrix equations in T+H v2.0

Various versions of T+H have been used for a wide range of investigations of gas production from hydrates in both oceanic deposits and in accumulations associated with the permafrost that cover the entire spectrum of hydrate types, e.g., Class 1 (Moridis et al., 2008), Class 2 (Moridis and Reagan, 2007, 2010a,b; Moridis et al., 2013; Reagan et al., 2014), Class 3 (Moridis and Reagan, 2007; Moridis et al., 2011), and Class 4 (Moridis and Sloan, 2007; Li et al., 2010; Moridis et al., 2011).

3 Model Description

3.1 Fundamental equations - Mass accumulation terms

Following the approach in Moridis (2014); Pruess et al. (1999, 2012), the components of the pore-filling media are broken into components labeled by κ. Let M^κ denote a mass density for component

κ. The balance of mass and heat dictates that, for every subdivided element or gridblock of the simulation domain, the following holds for each component κ:

$$\frac{\mathrm{d}}{\mathrm{d}t}\int_{V_n} M^\kappa \mathrm{d}V = \int_{\Gamma_n} \mathbf{F}^\kappa \cdot \mathbf{n}\,\mathrm{d}A + \int_{V_n} q^\kappa \mathrm{d}V, \tag{2}$$

where V_n is the volume of the subdomain n with differential $\mathrm{d}V$ [m^3]; M^κ is the mass accumulation of component κ [$\mathrm{kg}\cdot\mathrm{m}^{-3}$]; Γ_n is the surface of subdomain n with differential $\mathrm{d}A$ [m^2]; $\mathbf{F}^\kappa$ is the flux vector of component κ [$\mathrm{kg}\cdot\mathrm{m}^2\cdot\mathrm{s}^{-1}$]; $\mathbf{n}$ is the inward unit normal vector; and $\mathbf{q}^\kappa$ is the source/sink term of component κ [$\mathrm{kg}\cdot\mathrm{m}^3\cdot\mathrm{s}^{-1}$].

The non-isothermal hydrate system can be fully described by the appropriate mass and energy balance equations. The following components κ are considered: $\kappa = h$ for hydrate (for kinetic formation/dissociation only); w for H_2O; m for CH_4; i for a water-soluble inhibitor (salt or organic substance); and θ for heat. Heat is included in this list as a pseudo-component as it is tracked similarly to the mass balance equations. Note that hydrate behavior cannot be described isothermally. Thus, the maximum number of mass components is 4 for kinetic hydrate formation/dissociation corresponding to 5 equations. For equilibrium hydrate formation/dissociation, hydrate is a state of the H_2O+CH_4 system instead of a separate species, reducing the number of components and equations to 3 and 4, respectively.

Under equilibrium conditions, the mass accumulation terms M^κ for each component κ in Eq. 2 are given by

$$M^\kappa = \sum_{\beta=A,G,I,H} \phi S_\beta \rho_\beta X_\beta^\kappa \quad \kappa = w, m, i \tag{3}$$

where ϕ is the porosity, ρ is the density [$\mathrm{kg}\cdot\mathrm{m}^{-3}$]; S_β is the saturation of the phase; X_β^κ is the mass fraction of component κ in phase β. In hydrates, the mass components are partitioned among four possible phases β: H, denoting the solid-hydrate phase (components: m,w for equilibrium or h for kinetic); A for the aqueous phase (components: mainly w, but also containing dissolved m and/or dissolved i); G for the gaseous phase (components: mainly m, and vapor w); and I denoting the solid ice (component: w).

In the equilibrium model, each phase has the following constraints:

$$\beta = G : X_G^i = 0 \tag{4}$$

$$\beta = H : X_H^w = \frac{W^m}{W^h}, \quad X_M^m = 1 - X_H^w, \quad X_H^i = 0 \tag{5}$$

$$\beta = I : X_I^m = X_I^i = 0, \quad X_I^w = 1 \tag{6}$$

The terms W^m and W^h denote the molecular weights of the CH_4 and of the hydrate, respectively, reflecting the stoichiometry in Eq. 1. Under kinetic conditions, the mass accumulation terms M_κ in Eq. 2 are given by

$$M^\kappa = \sum_{\beta=A,G,H,I} \phi S_\beta \rho_\beta X_\beta^\kappa, \quad \kappa = w, m, h, i \tag{7}$$

In the kinetic model, the constraints for each phase are:

$$\beta = A : X_A^h = 0 \tag{8}$$

$$\beta = G : X_G^h = X_G^i = 0 \tag{9}$$

$$\beta = H : X_H^w = X_M^m = X_H^i = 0, \quad X_H^h = 1 \tag{10}$$

$$\beta = I : X_I^m = X_I^h = X_I^i = 0, \quad X_I^w = 1 \tag{11}$$

The model of Kim et. al (Kim et al., 1987; Clarke and Bishnoi, 2001) is used to describe the kinetic behavior of the hydrate mass component and phase (where $\kappa = m$ indexes into the methane component):

$$Q^m = \frac{\partial M^m}{\partial t} = -K_0 \exp\left(\frac{\Delta E_a}{RT}\right) F_A A \left(f_{eq} - f_v\right) \tag{12}$$

where K_0 is the intrinsic hydration reaction constant [kg m^{-2} Pa^{-1} s^{-1}]; ΔE_a is the hydration activation energy [J mol^{-1}]; R is the universal gas constant [8.314 J mol^{-1} K^{-1}]; F_A is an area adjustment factor [dimensionless]; A is the surface area participating in the reaction [m^2]; f_{eq} and f_v are the fugacities [Pa] at the equilibrium temperature T_{eq} and at temperature T, respectively.

The surface area is computed by assigning the hydrate saturation uniformly to the interstitial spaces of the porous medium. The original solid grain volume (assuming spherical grain) is determined as $V_p = 4\phi r_p^3/3$, where r_p is the grain radius [m]. Then, the number of voids N_V is assumed to be equal to the number of solid grains, and the corresponding void volume V_V is computed from

$$N_V = \frac{1-\phi}{V_p}, \quad V_V = \frac{\phi}{N_V}. \tag{13}$$

At the interface of pores and voids, the grain surface area is computed as $A_p = 4\pi r_p^2$, resulting in a total area (per unit volume) of $A_{TV} = N_V A_p$. Then, the void volume is assumed to vary linearly with r_V^3 where $r_V = 0.1547 r_p$ is a representative radius of a sphere inscribed in the interstitial space between the grains. A representative hydrate particle radius r_H and volume V_H are computed by

$$V_H = \frac{\phi S_H}{N_V}, \quad r_h = r_V \left(\frac{V_H}{V_V}\right)^{1/3} = r_V \, S_H^{1/3} \tag{14}$$

and the reactive area is computed by

$$A = f_A \, A_{TV} \left(\frac{r_H}{r_V}\right)^2 = f_A \, N_V \left(4 \, \phi \, r_p^2\right)^{1/3} S_H^{2/3}. \tag{15}$$

The area adjustment factor f_A accounts for the deviation of the interstitial volume from the assumption of grain sphericity, and can incorporate heterogeneity related to the hydrate "particle" size, shape, and saturation distribution. An estimate of r_p can be obtained from sieve analysis. Alternatively, given the intrinsic permeability k, the Kozeny-Carman equation estimates r_p by

$$r_p = \left[45k \frac{(1-\phi)^2}{\phi^3}\right]^{1/2}. \tag{16}$$

3.2 Fundamental equations - Heat accumulation terms

The heat accumulation term includes contributions from the rock matrix and all phases, and, in the kinetic model, is given by the equation

$$M_\theta = \int_{T_0}^{T} (1-\phi) \, \rho_R \, C_R \, dT + \sum_{\beta = A,G,H,I} \phi \, S_\beta \, \rho_\beta \, X_\beta \, U_\beta + Q_{diss}, \tag{17}$$

where

$$Q_{diss} = \begin{cases} \Delta\left(\phi \rho_H S_H \Delta H^0\right) & \text{for equilibrium dissociation} \\ Q_H \Delta H^0 & \text{for kinetic dissociation} \end{cases} \tag{18}$$

In the above equation, ρ_R is the rock density [kg m^{-3}]; C_R is the heat capacity of the dry rock [J kg^{-1} K^{-1}]; U_β is the specific internal energy of phase β [J kg^{-1}]; $\Delta()$ denotes a change; and ΔH^0

is the specific enthalpy of hydrate dissociation/formation [J kg^{-1}]. The specific internal energy of the gaseous phase is a very strong function of composition, related to the specific enthalpy of the gas phase H_G by

$$U_G = \sum_{k=w,m} X_G^\kappa u_G^\kappa + U_{dep} = \left(H_G - \frac{P}{\rho_G} \right), \tag{19}$$

where W_G^κ is the specific internal energy of component κ in the gaseous phase, and U_{dep} is the specific internal energy departure of the gas mixture [Jkg^{-1}]. The internal energy of the aqueous phase accounts for the effects of gas and inhibitor solution with

$$U_A = X_A^w u_A^w + X_A^m \left(u_A^m + u_{sol}^m \right) + X_A^i \left(u_A^i + u_{sol}^i \right) \tag{20}$$

where u_A^w, u_A^m, and u_A^i are the specific internal energies of H_2O, CH_4, and the inhibitor at the conditions in the aqueous phase, respectively; and u_{sol}^m and u_{sol}^i are the specific internal energies corresponding to the dissolution of CH_4 and of the inhibitor in water, respectively. The terms u_A^i and U_H are determined from

$$u_A^i = h_A^i - \frac{P}{\rho_i} = \int_{T_0}^{T} C_i \, \mathrm{d}T - \frac{P}{\rho_i} \tag{21}$$

$$U_H = H_H - \frac{P}{\rho_H} = \int_{T_0}^{T} C_H \, \mathrm{d}T - \frac{P}{\rho_H} \tag{22}$$

where T_0 is a reference temperature; h_A^i and H_H are the specific enthalpies of H_2O and hydrate (phase or component), respectively; and C_i and C_H are the temperature-dependent heat capacities of the inhibitor and the gas hydrate, respectively [J kg^{-1}K^{-1}].

3.3 Fundamental equations - Flux terms

The mass fluxes of water, CH_4 and inhibitor include contributions from the aqueous and gaseous phases:

$$\mathbf{F}^\kappa = \sum_{\beta=A,G} \mathbf{F}_\beta^\kappa, \quad \kappa = w, m, i \tag{23}$$

The contributions of the two immobile solid phases ($\beta = H, I$) to the fluid fluxes are zero. In the kinetic model, the mass flux of the hydrate component is zero as well.

For the aqueous phase ($\beta = A$), the phase flux F_A is described by Darcy's law:

$$\mathbf{F}_A = \rho_A \mathbf{v}_\beta = \rho_A \left[-\frac{k k_{rA}}{\mu_A} \nabla \Phi_A \right], \qquad \nabla \phi_A = \nabla P_A - \rho_A \mathbf{g} \tag{24}$$

where k is the rock intrinsic permeability [m^2]; k_{rA} is the relative permeability of the aqueous phase A [dimensionless]; μ_A is the phase viscosity [Pa s]; P_A is the phase pressure [Pa]; $\mathbf{v}_A$ is the velocity of the aqueous phase; and $\mathbf{g}$ is the gravitational acceleration vector [m s^{-2}]. The aqueous pressure P_A is related to the gas pressure P_G by

$$P_A = P_G - P_{cGW} \tag{25}$$

where P_{cGW} is the gas-water capillary pressure [Pa]. The gas pressure is equal to $P_G = P_G^m + P_G^w$ where P_G^m and P_G^w are the CH_4 and water vapor partial pressures [Pa] in the gas phase, respectively.

The CH_4 solubility in the aqueous phase is related through Henry's law,

$$P_G^m = H^m(T) \, Y_A^m, \tag{26}$$

where $H^m(T)$ [Pa] is the temperature- and salinity-dependent Henry's coefficient. As an option, the CH_4 solubility may also be determined from the equality of fugacities in the aqueous and the gas phase Moridis and Freeman (2014).

The mass flux of the gaseous phase ($\beta = G$) incorporates advection and diffusion contributions with

$$\mathbf{F}_G^\kappa = -k_0 \left(1 + \frac{b}{p_G}\right) \frac{k_{rG}\,\rho_G}{\mu_G} X_G^\kappa \left(\nabla p_G - \rho_G\,\mathbf{g}\right) + \mathbf{J}_G^\kappa, \qquad \kappa = w, m \tag{27}$$

where k_0 [m^2] is the absolute permeability at large gas pressures; and b [Pa] is the Klinkenberg (Klinkenberg, 1941) b-factor (appropriately expanded to account for Knudsen flow effects, as needed) accounting for gas slippage effects. The Klinkenberg b-factor is either provided as an input or computed using relations such as the correlation proposed by Jones (1972):

$$\frac{b}{b_r} = \left(\frac{k}{k_r}\right)^{-0.36} \tag{28}$$

where the subscript r denotes a reference medium with a known b-factor and k (e.g., see Wu et al. (1988)). Additional relations implemented in T+H are described by Moridis and Freeman (2014). The use of a Klinkenberg-type b-factor to desribe Knudsen flow is discussed later in this section.

The term $\mathbf{J}_G^\kappa$ in Eq. 27 is the diffusive mass flux of component κ in the gas phase [kg/(m^2s)]. Diffusive flux is an important term for long term studies due to the ultra-low permeability typically found in HBS, and thus Knudsen diffusion is included. The term $\mathbf{J}_G^\kappa$ in Eq. 27 is the diffusive mass flux of component κ in the gas phase [kg/(m^2s)] given by

$$\mathbf{J}_G^\kappa = -\phi\, S_G \underbrace{\left(\phi^{1/3} S_G^{7/3}\right)}_{\tau_G} D_G^\kappa\, \rho_G\, \nabla X_G^\kappa = -\phi\, S_G \tau_G\, D_G^\kappa\, \rho_G \nabla X_G^\kappa, \qquad \kappa = w, m \tag{29}$$

where D_G^κ is the multicomponent molecular diffusion coefficient of component κ in the gas phase in the absence of a porous medium [$m^2 s^{-1}$], and τ_G is the gas tortuosity [dimensionless]. The Millington and Quirk model (Millington and Quirk, 1961) was used to compute τ_G in Equation 29; additional models are discussed in Moridis and Pruess (2014). The diffusive mass fluxes of the water vapor and CH_4 gas are related through the relationship of Bird et al. (1960)

$$\mathbf{J}_G^w + \mathbf{J}_G^m = 0, \tag{30}$$

which ensures that the total diffusive mass flux of the gas phase is zero with respect to the mass average velocity. The total gas mass flux is the product of the Darcy velocity and density of the gas phase.

In the case of Knudsen flow, a Klinkenberg-type b-factor that is computed by the method of Florence et al. (2007)] and Freeman et al. (2011) is used to allow the gas flow computations described by Eq. 27:

$$\frac{b}{p_G} = (1 + \alpha_\kappa K_n)\left(1 + \frac{4K_n}{1 + K_n}\right) - 1, \tag{31}$$

where K_n is the Knudsen diffusion number [dimensionless] characterizing the deviation from continuum flow and accounting for the effect of the mean free path of gas molecules $\bar{\lambda}$ being comparable to the pore dimensions, computed by (Freeman et al., 2011)

$$K_n = \frac{\bar{\lambda}}{r_{pore}} = \frac{\mu_G}{2.81708\,\rho_G} \sqrt{\frac{\pi\, R\, T \phi}{2\, k\, W^m}}. \tag{32}$$

The term α_κ in Eq. 31 is determined from Karniadakis and Beskok (2002) by

$$\alpha_\kappa = \frac{128}{15\,\pi^2} \tan^{-1}(4\, K_n^{0.4}). \tag{33}$$

The Knudsen diffusion is important in media with pores smaller than few micrometers and at low pressures. The Knudsen diffusivity D_K [m^2/s] can be computed by (Freeman et al., 2011; Civan, 2008)

$$D_K = \frac{4\sqrt{k\,\phi}}{2.81708}\sqrt{\frac{\pi\,R\,T}{2\,M}} \qquad \text{or} \qquad D_K = \frac{kb}{\mu_G}. \tag{34}$$

In hydrate-free regions near the well, the methane gas phase usually exhibits flow that is turbulent. In this regime, turbulent flow is accounted for using the Forcheimer equation (Forchheimer, 1901; Wattenbarger and Ramey, 1968). The velocity $\mathbf{v}_G$ is computed from the solution of the quadratic equation

$$\nabla\Phi_G = -\left(\frac{\mu_G}{k\,k_{rG}}\mathbf{v}_\beta + F_T\,\rho_\beta\,\mathbf{v}_\beta\,|\mathbf{v}_\beta|\right), \tag{35}$$

in which F_T is the "turbulence correction factor" (Katz, 1959). The solution

$$\mathbf{v}_\beta = \frac{2\nabla\Phi_\beta}{\dfrac{\mu_\beta}{k\,k_{r\beta}} + \sqrt{\left(\dfrac{\mu_\beta}{k\,k_{r\beta}}\right)^2 + 4\,F_T\,\rho_\beta\,|\nabla\Phi_\beta|}} \tag{36}$$

is used in the equations of flow (24 and 27). There are various options to compute F_T (Moridis and Freeman, 2014).

The flux of components $\kappa = w, m, i$ in the aqueous phase is described by

$$\mathbf{F}_A^\kappa = X_A^\kappa \mathbf{F}_A + \mathbf{J}_A^\kappa, \tag{37}$$

where the diffusion term $\mathbf{J}_A^\kappa$ is

$$\mathbf{J}_A^\kappa = -\phi\,S_A\underbrace{\left(\phi^{1/3}\,S_A^{7/3}\right)}_{\tau_A} D_A^\kappa\,\rho_A\,\nabla X_A^\kappa = -\phi\,S_A\,(\tau_A)\,D_A^\kappa\,\rho_A\,\nabla X_A^\kappa, \tag{38}$$

where D_A^κ is the molecular diffusion coefficient of component κ in H_2O, and τ_A is the aqueous phase tortuosity.

The heat flux accounts for conduction, advection, and radiative heat transfer:

$$\mathbf{F}^\theta = -\bar{k}_\theta\nabla T + \sum_{\beta=A,G} h_\beta\mathbf{F}_\beta \tag{39}$$

where $\bar{k}_\theta$ is the composite thermal conductivity of the medium/fluid ensemble [W/(m K)] and h_β is the specific enthalpy of phase $\beta = A, G$ [$J\,kg^{-1}$]. Of the possible options to estimate $\bar{k}_\theta$, the following equation (based on the laboratory studies of Kneafsey et al. (2005)) is recommended for hydrated-bearing media:

$$\bar{k_\theta} = k_{\theta d} + \left(\sqrt{S_A} + \sqrt{S_H}\right)(k_{\theta w} - k_{\theta d}) + \phi\,S_I\,k_{\theta I}. \tag{40}$$

Here, $k_{\theta I}$, $k_{\theta w}$, and $k_{\theta d}$ are the thermal conductivities of the ice, the water-saturated, and the dry porous medium, respectively.

The specific enthalpy of the gas phase is computed as

$$H_G = \sum_{\kappa=w,m} X_G^\kappa\,h_G^\kappa + H_{dep}, \tag{41}$$

where h_G^κ is the specific enthalpy of component κ in the gaseous phase and H_{dep} is the specific enthalpy departure of the gas mixture [$J\,kg^{-1}$]. The specific enthalpy of the aqueous phase is estimated from

$$H_A = X_A^w\,h_A^w + X_A^m\,(h_A^m + H_{sol}^m) + X_A^i\left(h_A^i + H_{sol}^i\right), \tag{42}$$

where h_A^w, h_A^m, and h_A^i are the specific enthalpies of H_2O, CH_4, and the inhibitor at the aqueous phase conditions, respectively; and H_{sol}^m and H_{sol}^i are the specific enthalpy of dissolution [$J\,kg^{-1}$] of CH_4 and the inhibitor in the aqueous phase, respectively.

3.4 Fundamental equations - Sinks and sources

In sinks with specified mass production rate, withdrawal of the mass component κ is described by

$$\hat{q}^{\kappa} = \sum_{\kappa=A,G} X_{\beta}^{\kappa}\, q_{\beta}, \qquad \beta = w, m \tag{43}$$

where q_{β} is the production rate of phase β [$\mathrm{kg\,m^{-3}}$]. For source terms (well injection), the addition of a mass component κ occurs at desired rates $\hat{q}^{\kappa}$ ($\kappa = w, m$). Inhibitor injection can occur either as a rate as an individual mass component, $\hat{q}^{i}$, or as a fraction of the aqueous phase injection rate, i.e. $\hat{q}^{i} = X_A^i \hat{q}_A$ where X_A^i is the injected inhibitor mass fraction.

In the kinetic model, the additional sink/source terms corresponding to hydrate dissociation and release of CH_4 and H_2O in each element must be accounted for. The source term for CH_4 is $\hat{q}^{m} = Q^{m}$, where the production rate Q^{m} [$\mathrm{kg\,m^{-3}\,s^{-1}}$] is computed from Eq. 12 as

$$Q^{m} = -\frac{W^{m}}{W^{h}}\, Q^{h}. \tag{44}$$

Similarly, the source term for water (liquid or ice) is $\hat{q}^{w} + Q^{w}$, where the release of water Q^{w} is determined from the stoichiometry of Eq. 1:

$$Q^{w} = -\frac{N_H\, W^{w}}{W^{h}}\, Q^{h}. \tag{45}$$

Under equilibrium conditions, the rate of heat removal or addition includes contributions of fluid removal or addition as well as direct heat inputs or withdrawals q_d (e.g., microwave heating):

$$\hat{q}^{\theta} = q_d + \sum_{\beta=A,G} h_{\beta}\, q_{\beta}. \tag{46}$$

Under kinetic conditions, the rate of heat removal or addition is determined from

$$\hat{q}^{\theta} = q_d + \sum_{\beta=A,G} h_{\beta}\, q_{\beta} + Q^{h}\, \Delta H^{0}. \tag{47}$$

3.5 Thermophysical properties

Since the last published version of T+H, the thermophysical relations for methane gas hydrate have been improved by the additions described in Section 2. The thermophysical properties and parameters of the various states of water (i.e., state boundaries, density, enthalpy, viscosity, and thermal conductivity), including the transition Region II in the vicinity of the critical point, are provided by the correlations proposed by Wagner et al. (2000); International Association for the Properties of Water and Steam (IAPWS) (2012, 2011a,b, 2009, 2008, 2007). The thermal conductivity of ice is computed using the heat capacity polynomial equation with the coefficients reported in Yaws (1999). The properties of the gas phase are provided by one of three cubic equations of state: (a) the Peng-Robinson equation Peng and Robinson (1976), (b) the Soave-Redlich-Kwong equation (Soave, 1972), and (c) the standard Redlich-Kwong equation (Redlich and Kwong, 1949). The Lee-Kesler method (Lee and Kesler, 1975) is used to compute the enthalpy of hydrocarbons. The gas viscosity and thermal conductivity using the high-pressure method of Chung et al. (1988) or the Friction Theory of Quiñones-Cisneros et al. (2000). Binary diffusivities are computed by the method of Fuller et al. (1969) and Riazi and Whitson (1993).

The hydration number N_H and the thermal properties of the CH_4-hydrate are input functions of temperature. The hydrate density ρ_H is computed from the Ballard equation:

$$\rho_H = \left[v_0 \exp\left(\alpha_1 \Delta T + \alpha_2 \Delta T^2 + \alpha_3 \Delta T^3 + \alpha_4 \Delta P \right) \right]^{-1} \tag{48}$$

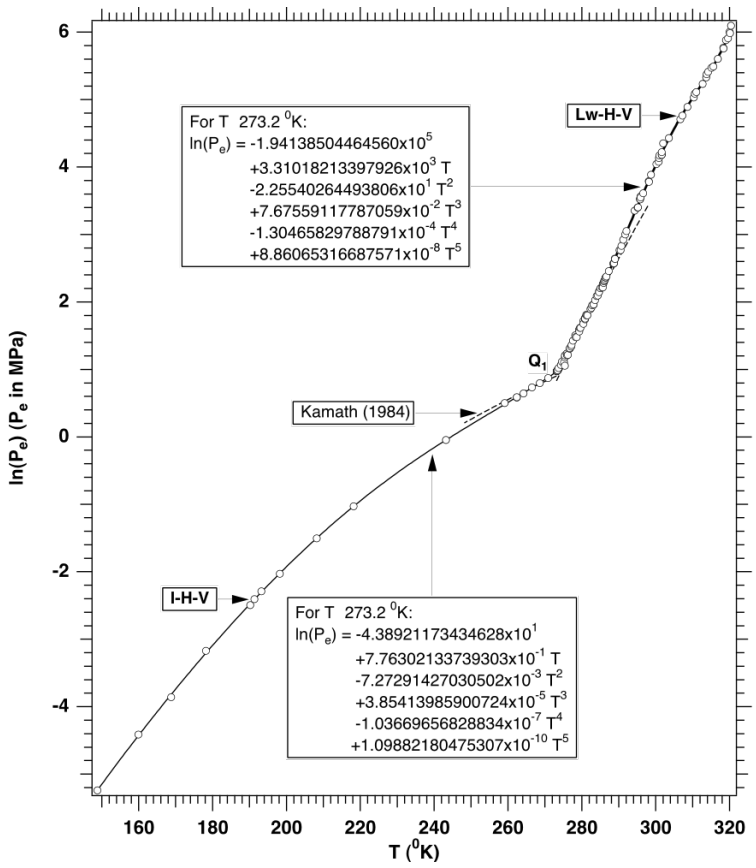

Fig. 1 CH_4-hydrate: relationship of the equilibrium hydration pressure P_e to the temperature T (Moridis, 2003)

(Ballard, 2002) in which the temperature change is $\Delta T = T - T_0$, the pressure change is $\Delta P = P - P_0$, with reference temperature $T_0 = 298.15$K, and pressure $P_0 = 10^5$ Pa; the coefficients are given by $\alpha_1 = 3.384\,96 \times 10^{-4}\,\mathrm{K}^{-1}$, $\alpha_2 = 5.400\,99 \times 10^{-7}\,\mathrm{K}^{-2}$, $\alpha_3 = -4.769\,46 \times 10^{-11}\,\mathrm{K}^{-3}$, $\alpha_4 = 1 \times 10^{-10}\,\mathrm{Pa}^{-1}$, and the specific volume is $v_0 = 1000\,W^m/(22.712 N_H)$ (Ballard, 2002). The specific enthalpy of the solid hydrate H_H [J/kg] is estimated from the general equation $H_H = \int_{T_{0H}}^{T} C_H \mathrm{d}T$, where $T_{0H} = 273.15\,\mathrm{K}$ and $C_H = 2,100$ J/kg/K (Ballard, 2002).

Of particular interest are the pressures and temperatures of the Lw-H-V and I-H-V three-phase lines in the H_2O-CH_4 diagram which delineate the limits to hydrate formation/dissociation. The relationship between the equilibrium hydration pressure P_e and the equilibrium hydration temperature T_e can be obtained from two sources. The first involves the parametric equation (Moridis, 2003) in Figure 1 which delineates the spectrum of hydrate formation/dissociation over both three-phase lines. The second is the regression equation of Kamath that is only applicable to the Lw-H-V line (Kamath, 1984).

There are no specific measurements of the equilibrium P-T relationship along the I-H-Lw and the I-V-Lw phase lines (see Figure 1) of a $H_2O{-}CH_4$ system, but it is considered to follow the solidus line of the water-ice system (International Association for the Properties of Water and Steam (IAPWS), 2007):

$$P = P_Q - 6.26 \times 10^5 \left(1.0 - T_d^{-3}\right) + 1.97135 \times 10^5 \left(1.0 - T_d^{21}\right) \tag{49}$$

where P is in Pa, $T_d = T/273.16$ [K], P_Q [Pa] is the pressure at the hydrate quadruple point (Fig. 1). Finally, $T = 273.16$ K and is constant along the I-V-Lw line.

3.6 Geoemechanical dependence on ϕ and k

In some cases, the full solution of the geomechanics using Millstone is not necessary, and T+H can use simplified relationships to adjust the porosity. As it is significantly cheaper computationally, a scoping simulation using this simplified approach is typically run as a first pass. Multiple approaches have been used. For hydrate bearing sediments, the most applicable relation describes the ϕ-dependence on P in unconsolidated media that gain significant mechanical strength from the presence of solid phases such as ice or hydrates (Moridis, 2014), in which

$$\phi = \phi_0 F_{PT}, \quad where \quad F_{PT} = \exp\left(\alpha_p \Delta P + \alpha T \Delta T\right), \tag{50}$$

where α_T is the thermal expansivity of the porous medium [K^{-1}] and α_p is the pore compressibility [Pa^{-1}], which can be either a fixed number or a function of pressure (Moridis et al., 2008, 2009, 2012). The factor α_P can also account for solid phases as function of $S_S = S_H + S_I$ with the empirical model:

$$\alpha_p = \exp\left\{\log \alpha_{PL} + (\log \alpha_{PU} - \log \alpha_{PL})\left[1 - B_x(2.25, 2.25, S_S^t)\right]\right\}, \tag{51}$$

where

$$S_S^t = \frac{S_S - S_{min} + \delta}{S_{Smax} - S_{Smin} + 2\delta}, \tag{52}$$

α_{PL} is the lower limit of the medium compressibility (corresponding to the full strengthening effect of cementing solid phases), α_{PU} is the upper limit of the medium compressibility (corresponding to the absence of cementing phases), B_x is the incomplete beta function, S_{Smin} is the largest solid saturation at which $\alpha_P = \alpha_{PU}$, S_{Smax} is the lowest solid saturation at which $\alpha_P = \alpha_{PL}$, and δ is a smoothing factor. Eq. 51 is based on geomechanical and geophysical data derived from laboratory and field observations. For example, this approach may be adequate in shallow stiff permafrosts. In Part 2 of this series, the complete geomechancis treatment will be described, in which ϕ is incrementally updated using the mechanical strain. In Part 3, T+H is run without Millstone using this simplified approach to compare with the fully detailed TOUGH+Millstone simulation.

The $\phi - k$ relationship in the matrix is described by the empirical equation (Rutqvist and Tsang, 2002):

$$\frac{k}{k_0} = \exp\left[\gamma\left(\frac{\phi}{\phi_0} - 1\right)\right], \tag{53}$$

where γ is an empirical reduction factor that ranges between 5 (for soft unconsolidated media) and 29 (for highly consolidated media). Note that the equations described apply to ϕ and k changes when the P and T changes are small; large changes necessitate coupling with a geomechanical solver, which is responsible for computing changes to ϕ as well as the geometry of the gridblock. The change to the gridblock volume V_n is the dominant source for geomechanical effects.

3.7 Effects of solid phases and wettability

Hydrate behavior includes the evolution of solid phases yielding significant effects on ϕ and k. The simplest model conceptualizes porous media as bundles of capillary tubes which implies a power law dependence of permeability on porosity,

$$\frac{k}{k_0} = F_{\phi S} = \left(\frac{\phi}{\phi_0}\right)^n \tag{54}$$

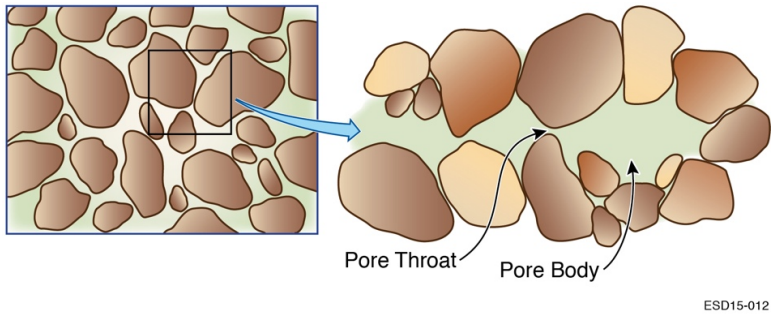

Fig. 2 Schematic of pore channels showing convergent-divergent geometry with a succession of pore throats and pore bodies

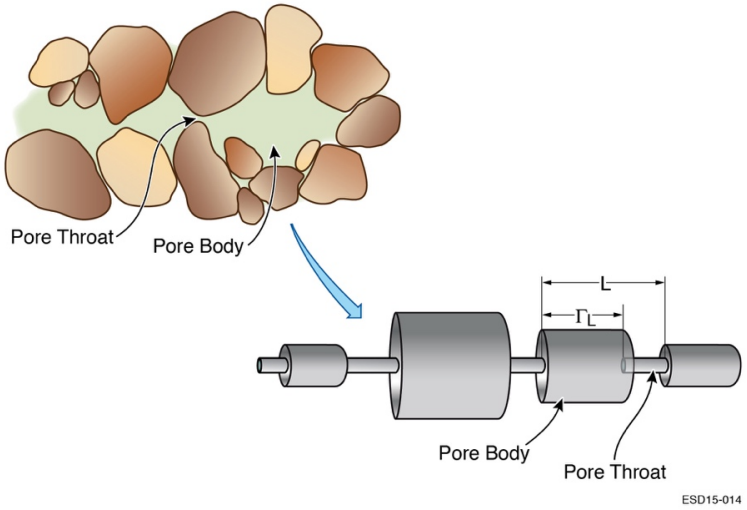

Fig. 3 Tubes-in-series model of pore channels.

where $F_{\phi S}$ is a *permeability adjustment factor* that describes the effects of the presence of solid phases other than the medium grains and changes in porosity on permeability, and the subscript "0" denotes properties at a solid-free reference state. Note that the effect of P and T is a separate issue. The exponent n has been reported in the range from 2 to 3 (Phillips, 1991), describing a mild dependence of k on ϕ that suggests solid phases forming at the center of the pores.

In media with inter-granular porosity, pore channels generally have a convergent-divergent geometry, as illustrated in Figure 2. If solids are deposited the pore walls or in the throats, small depositions can give rise to a dramatic decrease in k and even $k = 0$ with throat clogging (Pape et al., 1999; Xu et al., 2004; Morrow et al., 1981; Vaughan, 1987). This can be understood by the 'tubes-in-series' model shown in Figure 3. A non-zero 'critical porosity' ϕ_c is introduced resulting in the following $k - \phi$ relationship (Xu et al., 2004; Verma and Pruess, 1988):

$$\frac{k}{k_0} = F_{\phi S} = \left(\frac{\phi - \phi_c}{\phi_0 - \phi_c}\right)^n \tag{55}$$

This relation indicates a very strong dependence of k on ϕ, with exponents as large as $n = 10$ or more (Pape et al., 1999). The solid-phase effect on the k-ϕ relationship merits further fundamental research.

In multiphase flow, the effect of the interference of any phase on the flow of any other phase is represented by the phase relative permeabilities. The effective permeability k_β for phase β is given by

$$k_\beta = k\, k_{r\beta} \quad \text{where} \quad k = k_0\, F_{\phi S} = k_{00}\, k_{rr}\, F_{\beta S} \tag{56}$$

and k_{rr} is the relative magnitude that relates the permeability k_0 of a given medium to k_{00} of the reference medium at the same P and T. The term k_rr is introduced when insufficient data is available and an analogue reference medium is needed. With the same medium as reference, $k_{rr} = 1$, and, with a different reference, $k_{rr} = k_0/k_{00}$. The factor $F_{\phi s}$ describes the effect of solid phases: $F_{\phi s} = 1$ if $S_S = 0$. Surface tension effects between phases yield capillary pressures P_{cap} which describe the difference between the wetting (aqueous) and the non-wetting (gas) phase and are dependent upon the pore size distribution (Moridis and Pruess, 2014). The models of van Genuchten (1980); Corey (1954); Stone (1970); Parker et al. (1987); Brooks and Corey (1966) are used to compute relative permeability and capillary pressure.

The relations between porosity, permeability, and the formation of solid phases are difficult to characterize. Multiple relations are included in T+H and selected depending on how much data is available for a given system. Formation of solid phases will alter the pore size distribution, generally reducing pore sizes and increasing capillary pressures. Without detailed information on these effects, T+H involves a phenomenological approach that relates P_{cap} to ϕ and k through the Leverett J-function (Leverett, 1941):

$$P_{cap}(S_A) = \sqrt{\frac{k_{00}\,\phi}{k\,\phi_{00}}}\, P_{cap,00} \tag{57}$$

where $P_{cap,00}$ is the capillary pressure corresponding to a reference medium at the reference conditions with permeability and porosity k_{00} and ϕ_{00}, respectively; and $S_S = S_H + S_I = 0$. When $S_S > 0$, the fraction of pore space available to fluid phases is $S_A + S_G$, with the constraint

$$S_A + S_G = 1 - S_S. \tag{58}$$

The total current porosity ϕ and the active porosity ϕ_a available to fluids are then defined as

$$\phi_a = \underbrace{(F_{pt}\,\phi_{rr}\,\phi_{00})}_{\phi}\,(S_A + S_G) \Rightarrow \frac{\phi_a}{\phi_{00}} = F_{pt}\,\phi_{rr}\,(S_A + S_G) = F_{pt}\,\phi_{rr}\,(1 - S_S) \tag{59}$$

where the term F_{pt} is the porosity adjustment factor that accounts for the effects of P and T on ϕ (obtained either from Eq. 50 or from a geomechanical model). The argument in the capillary pressure function $P_{cap,0}$ on the righthand side of Eq. 57 is the aqueous saturation S_A; in a medium with $S_S > 0$, S_A is adjusted to the *scaled* saturation

$$S_A^* = \frac{S_A}{S_A + S_G} \tag{60}$$

From Eq. 56, the partitioning of k_β of phase β into separate dependencies on porosity, solid saturation, and fluid saturation leads to a conceptual ambiguity in the representation of k-reduction from solid deposition. Hydrate and ice formation must begin to form in the water-filled portion of the pore space, but solid crystals may grow into primarily gas-filled pores. Without further information, it is not possible to ascertain the applicability of Eqs. 55 or 56, and appropriate parameters are lacking.

T+H includes two proposed alternative models to describe the wettability processes ($k_{r\beta}$ and P_{cap}) in hydrate- and/or ice-bearing media (Moridis and Pruess, 2014; Moridis, 2003; Moridis et al., 2009, 2012). The "Original Porous Medium" (OPM) model, is based on the treatment of (a) ϕ as independent from the emergence of hydrates or ice but still dependent on P and T, (b) k_0 as independent to the evolution of the solid phases, and (c) the relative permeability for fluid flow

controlled by the phase saturations. The "Evolving Porous Medium" (EPM) models, considers the evolution of the solid phases (hydrate and ice) as creation of a new porous medium with continuously changing ϕ_0 and k_0, whose pore space is only occupied by the aqueous and gas phases.

The permeability adjustment factor (Eq. 56) is computed using

$$F_{\phi_S} = k_{r\phi}\, k_{rS}, \tag{61}$$

where $k_{r\phi}$ is the permeability ϕ-factor that describes the dependence of ϕ and k_{rS} is the permeability S-factor that relates reduction in the k_0 to the presence of solid phases. In the OPM model, $k_{rS} = 1$ for small changes in P, T and S_S. When ϕ changes are accounted for,

$$k_{r\phi} = \exp\left[\gamma\left(F_{PT} - 1\right)\right], \tag{62}$$

otherwise, $k_{r\phi} = 1$. γ and F_{PT} are as discussed in Eqs. 50 and 55. In the OPM model P_{cap} is estimated from Eq. 57, in which:

- $\phi/\phi_{00} = \phi_{rr} F_{PT}$ is computed from Eq. 50,
- $k_{00}/k = 1/k_{rr} k_{r\phi}$ is computed from Eqs. 56 and 62, and
- $P_{cap,00}$ is computed with S_A^* from Eq. 60

For large changes in P, T and S_S, the needed properties are calculated from the geomechanical model. The final expression for estimating the capillary pressure in the OPM model is:

$$P_{cap} = \sqrt{\frac{\phi_{rr}\, F_{PT}}{k_{rr}\, k_{r\phi}}}\, P_{cap,00}(S^*). \tag{63}$$

While there are two different EPM models in T+H, the authors recognize that a better model needs to be developed for hydrate systems using further theoretical, laboratory, and field studies. The evolving intrinsic permeability in EPM #1 Model is estimated by using (Moridis, 2014; Moridis and Pruess, 2014)

$$k_{rS} = \frac{1}{2}\left[k_{rA}(S_A = 1 - S_S) + k_{rG}(S_G = 1 - S_S)\right] \tag{64}$$

in Eq. 61, thus providing a simple estimate of the permeability ϕ-factor. The phase effective permeabilities are computed using Eq. 56, in which:

- $k_{r\beta}$ is computed based on the scaled saturations from Eq. 60,
- $F_{\phi S}$ is computed from Eq. 60,
- $k_{r\phi}$ is computed from Eq. 62, and k_{rS} is computed from Eq. 64.

The capillary pressure in the EPM #1 model is estimated using Eq. 57 using:

- ϕ_a/ϕ_{00}, computed from Eq. 59, is used instead of ϕ/ϕ_{00},
- $k_{00}/k = 1/k_{rr} F_{\phi S}$ is computed from Eqs. 59 and 60,
- $k_{r\phi}$ is computed from Eq. 62, and k_{rS} is computed from Eq. 64.

The final expression for estimating the capillary pressure in the EPM #1 model is

$$P_{cap} = \sqrt{\frac{\phi_{rr}\, F_{PT}\,(1 - S_S)}{k_{rr}\, k_{r\phi}\, k_{rS}}}\, P_{cap,00}(S^*). \tag{65}$$

The difference between the EPM #2 and EPM #1 models is the k_{rS} estimate. In the EPM #2 model, the quantity $F_{\phi S} = k_{r\phi} k_{rS}$ in Eq. 60 is provided by Eq. 56, leading to

$$k_{rS} = \left[\frac{\phi_0(1 - S_S) - \phi_C}{\phi_0 - \phi_C}\right]^n. \tag{66}$$

As in the OPM case, the EPM equations are applicable to small P, T, and S_S changes, requiring the geomechanical model for large changes.

Table 1 Primary Variables in Equilibrium Hydrate Simulations without Inhibitor

Phase	State Identifier	Primary Variable 1	Primary Variable 2	Primary Variable 3
1- Phase: G	**Gas**	P_G	Y_G^m	T
1- Phase: A	**Aqu**	P	X_A^m	T
2- Phase: A+G	**AqG**	P_G	S_A	T
2- Phase: I+G	**IcG**	P_G	S_I	T
2- Phase: H+G	**GsH**	P_G	S_G	T
2- Phase: A+H	**AqH**	P	S_A	T
2- Phase: A+I	**AqI**	P	S_A	X_A^m
2- Phase: I+H	**IcH**	P	S_I	T
3- Phase: A+H+G	**AGH**	S_G	S_A	T
3- Phase: A+I+G	**AIG**	P_G	S_A	S_G
3- Phase: A+I+H	**AIH**	P	S_A	S_G
3- Phase: I+G+H	**IGH**	S_G	S_I	T
Quadruple Point I+H+A+G	**QuP**	S_G	S_A	S_I

(Note: If an inhibitor is present, X_A^i becomes the 3rd primary variable, and the 3rd becomes the 4th.)

4 T+H Numerical Formulation and Code Capabilities

4.1 States and primary variables

The previous section details the system of equations that define the dynamics for the multiphse, multicomponent system. Up until this point, it has not been stated *which* variables are being solved more. Due to the complex nature of these equations, it is difficult to pick good variables to describe the state of the system, especially for the many different phase combinations. Thus, we are left with a set of difficult to solve differential algebraic equations,

$$\frac{\mathrm{d}}{\mathrm{d}t}\int_{V_n} M^\kappa(x_n)\mathrm{d}V = \int_{\Gamma_n} \mathbf{F}^\kappa(x_n)\cdot\mathbf{n}\,\mathrm{d}A + \int_{V_n} q^\kappa(x_n)\mathrm{d}V, \tag{67}$$

where x_n is the vector of primary variables for the gridblock n. It is necessary to change which system values are the primary variables in different phase combinations, as certain values that are useful in one phase cannot uniquely describe the system in another phase. The physical properties enumerated above cannot M cannot be solved for any choice of primary variables. There is no natural correspondence between any of the equations and any single one of the primary variables.

A total of 26 states (phase combinations) covering the entire phase diagram in Figure 1 are described in T+H. Of those, 13 correspond to the equilibrium hydration reaction option, and 13 to the kinetic hydration reaction option. The primary variables (i.e. the variables that are necessary and sufficient to uniquely define each state of the system) used for the various phase states without inhibitor are listed in Tables 1 and 2. For systems with an inhibitor, mass fraction of the inhibitor in the aqueous phase, X_A^i is an additional primary variable. The option set for both equilibrium or kinetic hydration reactions is complete, although some of the phase states are only feasible under laboratory conditions and difficult to reach during gas production from natural hydrate deposits.

4.2 Numerical Discretization

The continuum Eq. 2 is discretized in space using the integral finite difference method (IFDM) (Edwards, 1972; Narasimhan and Witherspoon, 1976; Narasimhan et al., 1978). The volume averages are defined by

$$\int_{V_n} M\mathrm{d}V = V_n M_n, \tag{68}$$

Table 2 Primary Variables in Kinetic Hydrate Simulations without Inhibitor

Phase	State Identifier	Primary Variable 1	Primary Variable 2	Primary Variable 3	Primary Variable 4
1- Phase: G	**Gas**	P_G	Y_G^m	S_H	T
1- Phase: A	**Aqu**	P	X_A^m	S_H	T
2- Phase: A+G	**AqG**	P_G	S_A	S_H	T
2- Phase: I+G	**IcG**	P_G	S_I	S_H	T
2- Phase: H+G	**GsH**	P_G	S_A	S_I	T
2- Phase: A+H	**AqH**	P	S_A	X_A^m	T
2- Phase: A+I	**AqI**	P	S_A	X_A^m	T
2- Phase: I+H	**IcH**	P	S_I	S_G	T
3- Phase: A+H+G	**AGH**	P_G	S_A	S_G	T
3- Phase: A+I+G	**AIG**	P_G	S_A	S_H	S_G
3- Phase: A+I+H	**AIH**	P	S_A	S_I	T
3- Phase: I+G+H	**IGH**	P_G	S_G	S_I	T
Quadruple Point I+H+A+G	**QuP**	P_G	S_A	S_G	S_I

(Note: If an inhibitor is present, X_A^i becomes the 4th primary variable, and the 4th primary variable (listed in this table) becomes the 5th primary variable.)

where M is a volume-normalized extensive quantity, and M_n is the average value of M over a volume V_n. Surface integrals are approximated as a discrete sum of averages over surface segments A_{nm}:

$$\int_{\Gamma_n} \mathbf{F}^k \cdot \mathbf{n} \mathrm{d}\Gamma = \sum_m A_{nm} F_{nm}. \tag{69}$$

Here F_{nm} is the average value of the (inward) normal component of $\mathbf{F}$ over the surface segment A_{nm} between volumes V_n and V_m. The discretization is illustrated in Figure 4. The discretized flux is expressed in terms of (a) the upstream mobility λ_{nm} evaluated at the facets of the elements and (b) the pressures at the center of the elements V_n and V_m. The mobile values are upstream-weighted where necessary. For the basic Darcy flux term in Eq. 24, we have

$$F_{\beta,nm} = -\underbrace{k_{nm}\left[\frac{k_{r\beta}\,\rho_\beta}{\mu_\beta}\right]}_{\lambda_{nm}}\left[\frac{P_{\beta,n}-P_{\beta,m}}{D_{nm}} - (\rho_\beta\, g)_{nm}\right] \tag{70}$$

where the subscripts (nm) denote a suitable averaging at the interface between grid blocks n and m (e.g. interpolation, harmonic weighting, or upstream weighting). $D_{nm} = D_n + D_m$ is the distance between the nodal points n and m, and g_{nm} is the component of gravitational acceleration in the direction from m to n. The term in the underbrace λ_{nm} is upstream weighted to be evaluated at the center of the facet.

Substitution of the discrete surface and volume integrals into the formulation yields a set of first-order ordinary differential equations describing the mass balance of component κ and the heat balance (θ) in time:

$$\frac{\mathrm{d}M_n^\eta}{\mathrm{d}t} = \frac{1}{V_n}\sum_m A_{nm}\, F_{nm}^\eta + q_m^\eta; \quad \eta = \kappa, \theta. \tag{71}$$

The time derivatives are approximated using the backward Euler method that is first-order accurate and L-stable. The following set of coupled non-linear, algebraic equations for residuals R_n^η result from including the temporal discretization:

$$R_n^{\kappa,k+1} = M_n^{\kappa,k+1} - M_n^{\kappa,k} - \frac{\Delta t}{V_n}\left(\sum_m A_{nm} F_{nm}^{\kappa,k+1} + V_n q_n^{\kappa,k+1}\right) = 0. \tag{72}$$

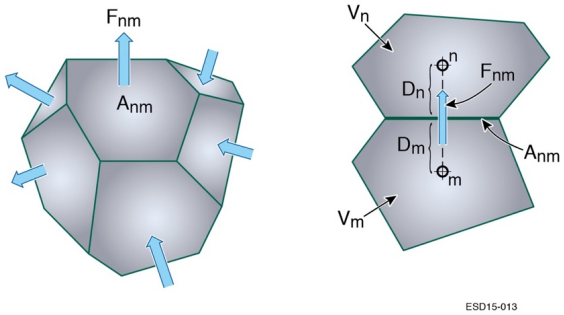

Fig. 4 Illustration of the connected volumes mesh for the IFDM.

For each volume V_n, there are N_η equations, so that for a system discretized into N_E grid blocks there are $N_\eta \times N_E$ coupled non-linear equations. Eq. 72 is solved fully implicitly for each gridblock's primary variables x_n, with all parameters, fluxes, and sink and source terms evaluated at t_{k+1}.

4.3 Solution of Discretized Equations

The unknowns are the $N_\eta \times N_E$ independent primary variables $\{x_i; i = 1, ..., N_\eta N_E\}$ which completely define the state of the flow system at t_{k+1}. These equations are solved by the Newton-Raphson method, the iterations of which are indexed by p. Expanding Eq. 72 at iteration step $p+1$ in a Taylor series in terms of the properties and conditions at index p yields

$$R_n^{\eta,k+1}\left(x_{i,p+1}\right) = R_n^{\eta,k+1}\left(x_{i,p}\right) + \sum_i \left[\frac{\partial R_n^{\eta,k+1}}{\partial x_i}\right]_p \left(x_{i,p+1} - x_{i,p}\right) \tag{73}$$

In T+H, all terms $\partial R_n/\partial x_i$ in the Jacobian matrix of Eq. 65 are evaluated by numerical differentiation. Iteration is continued until the residuals are reduced below a preset convergence tolerance:

$$\left|\frac{R_{n,p+1}^{\eta,k+1}}{M_{n,p+1}^{\eta,k+1}}\right| \leq \epsilon_1. \tag{74}$$

The default relative convergence criterion is $\epsilon_1 = 10^{-5}$. When the accumulation terms are smaller than ϵ_1, the following absolute convergence criterion (with a default value of $\epsilon_2 = 1$) is imposed:

$$\left|R_{n,p+1}^{\eta,k+1}\right| \leq \epsilon_1\epsilon_2. \tag{75}$$

5 Implementation

T+H (Moridis, 2014; Moridis and Pruess, 2014) is written in object oriented FORTRAN 2003 with cross-platform portability. The solution of the Jacobian matrix has been improved by including the the LIS (Nishida, 2010) and PETSc (Balay et al., 2014) matrix solvers. The simulations described in this series were primarily solved using LIS's stabilized Biconjugate gradient Krylov solver with an incomplete LU decomposition preconditioner, which has been determined to be the best option for the non-symmetric, non-positive-definite Jacobian matrices that arise from the numerical methods described.

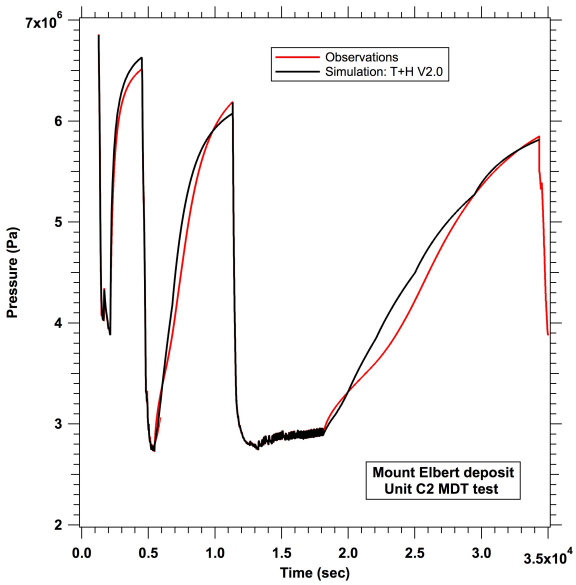

Fig. 5 Experimental results duplicated from Anderson et al. (2008)

6 Validation and Verification

Because the hydration reaction in porous media is complex, involving several coupled (physical, chemical and thermodynamic) strongly non-linear processes, there are no analytical solutions of benchmark problems. Validation and verification is thus achieved through comparisons to laboratory and field studies and to results obtained by previously validated simulators.

The previously validated T+H V1.0 was used for comparison. The first verification problem involved the analysis of a short-term field test of depressurization-induced hydrate dissociation that had been conducted in February of 2007 at the the Mount Elbert location in North Slope, Alaska. The collected data from the well were used in a code comparison study that was conducted by several different teams and involved T+H V1.0 and other hydrate codes. The reservoir properties and conditions and specifics of the code comparison study are documented in Anderson et al. (2008, 2011). Figure 5 shows a comparison between measurements and optimized numerical predictions that involve optimized parameters determined through the history matching process that had been followed in Anderson et al. (2008). The simulated pressure response using T+H V2.0 is very close to the field observations, and practically identical to the T+H V1.0 results (Anderson et al. (2008), Figure A5), from which they differ only in the 4th decimal place and beyond, with the newest simulation executed about twice as fast.

The second verification problem involves the description of lab-scale gas production tests using natural cores of hydrate-bearing media undergoing depressurization-inducing dissociation. These laboratory tests were conducted by Kneafsey and Moridis (2014) under tightly controlled conditions that included independent testing of the core media properties and X-ray computed tomography (CT) to examine the gas hydrate-bearing sediment structure and the spatial distribution of the hydrate saturation. In the original study, the simulations were conducted using T+H V1.0 and V1.2, and led to the determination of the porosity and hydrate saturation in the two core subdomains identified through analysis of the CT scans. Figure 6 shows a comparison of the amount of the released gas measured to both the older (T+H v1.0 and v1.2) and the newer (T+H v2.0) results obtained with the optimized parameters. The numerical predictions are practically identical, with T+H v2.0 executing about twice as fast.

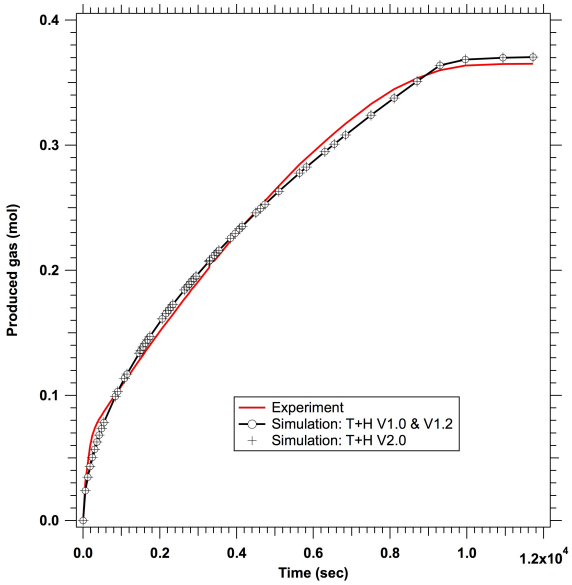

Fig. 6 Experimental results from Kneafsey and Moridis (2014).

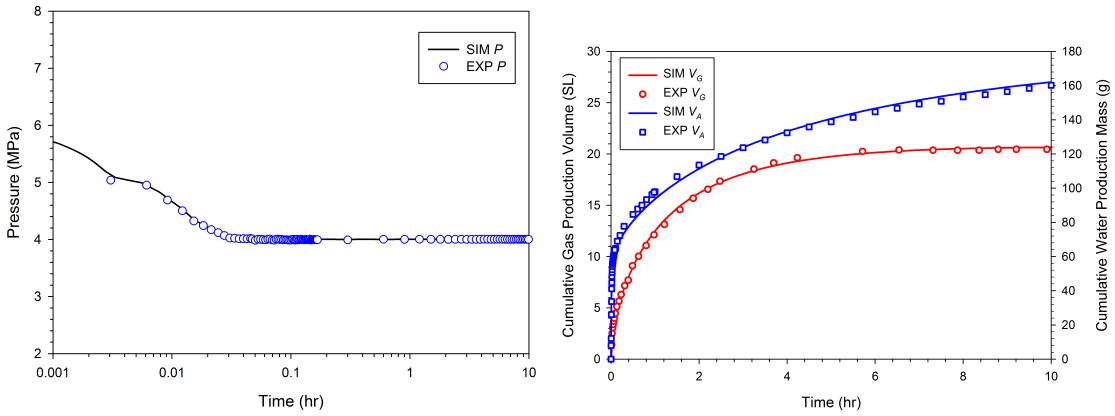

Fig. 7 Experimental results from Yin et al. (2018a,b).

The third verification problem describes the dissociation of a laboratory-created hydrate-bearing sand core. The formation is performed by the multi-step prcess described in detail by Yin et al. (2018a). The ensuing dissociation test was depressurization-driven, and is described in minute detail in Yin et al. (2018b). The dissociation process was reproduced numerically and fully analyzed using T+H v2.0 in a process involving inverse modeling (via history-matching) to determine the optimal values of key properties and parameters. The right of Figure 7 shows an excellent agreement between the measurements and the predictions of the produced volumes of gas and water during the dissociation experiments. The same excellent agreement between measurements and numerical predictions is observed in the evolution of pressure in the left of Figure 7. Note that because of the limited duration of the laboratory experiments (Kowalsky and Moridis, 2007), the simulations in the second and third verification problem were conducted using kinetic (as opposed to equilibrium) dissociation conditions.

7 Summary

In this series, we document the development and use of the TOUGH+Millstone simulator, which involves a coupling of the fully implicit TOUGH+HYDRATE v2.0 (T+H) simulator, describing flow, thermal, and chemical processes in hydrate-bearing media, with the Millstone v1.0 geomechanical model to describe the corresponding geomechanical response. In the first paper of this series, we discuss the T+H V2.0 simulator, a numerical simulator designed to describe the flow and thermal behavior of hydrate-bearing geologic media and a significant expansion of earlier versions. In the absence of analytical solutions for hydrate systems, the verification process of the T+H V2.0 code involves comparisons to numerical results from older versions of the code that had been used in code comparison studies (against other codes) and in the analysis of laboratory studies under tightly controlled conditions. In the second part of this series we describe Millstone v1.0, a new geomechanical framework that is the second component of the TOUGH+Millstone simulator. The combined simulator is applied to a real-world production analysis of a multilayered hydrate reservoir in the third and final part of the series.

Acknowledgments

This work was supported by the Assistant Secretary for Fossil Energy, Office of Natural Gas and Petroleum Technology, through the National Energy Technology Laboratory, under the U.S. Department of Energy, Contract No. DE-AC03-76SF00098, and also through a funded collaboration with Chevron.

References

K. A. Kvenvolden, Methane hydrate–a major reservoir of carbon in the shallow geosphere, Geo Chem 71 (1988) 41–51.

E. D. Sloan, C. Koh, Clathrate Hydrates of Natural Gases, Taylor and Francis, Inc., Boca Raton, FL, 3rd edition edition, 2008.

G. J. Moridis, M. B. Kowalsky, K. Pruess, TOUGH+HYDRATE v1.0 User's Manual: A Code for the Simulation of System Behavior in Hydrate-Bearing Geologic Media, Technical Report LBNL-0149E, Lawrence Berkeley National Laboratory, 2008.

G. J. Moridis, J. A. Apps, K. Pruess, L. Myer, EOSHYDR: A TOUGH2 Module for CH4-Hydrate Release and Flow in the Subsurface, Technical Report LBNL-42386, Lawrence Berkeley National Laboratory, 1998.

G. J. Moridis, Numerical studies of gas production from methane hydrates, SPE Journal 32 (2003) 359–370.

G. J. Moridis, T. Collett, Gas production from class 1 hydrate accumulations (section i, chapter 6), in: C. Taylor, J. Qwan (Eds.), Recent Advances in the Study of Gas Hydrates, Kluwer Academic/Plenum Publishers, 2004, pp. 75–88.

G. J. Moridis, T. Collett, S. Dallimore, T. Satoh, S. Hancock, B. Weatherhill, Numerical studies of gas production from several methane hydrate zones at the mallik site, mackenzie delta, canada, Journal of Petroleum Science and Engineering 43 (2004) 219–239.

G. J. Moridis, M. B. Kowalsky, K. Pruess, TOUGH-Fx/HYDRATE v1.1 User's Manual: A Code for the Simulation of System Behavior in Hydrate-Bearing Geologic Media, Technical Report LBNL-58950, Lawrence Berkeley National Laboratory, 2005.

H. C. Kim, P. R. Bishnoi, R. A. Heideman, S. S. H. Rizvi, Kinetics of methane hydrate decomposition, Chem Eng. Sci 42 (1987) 1645–1653.

M. Clarke, P. R. Bishnoi, Determination of activation energy and intrinsic rate constant of methane gas hydrate decomposition, Can. J. of Chem. Eng. 79 (2001) 143–147.

549 G. J. Moridis, M. Kowalsky, K. Pruess, Depressurization-induced gas production from class 1
550 hydrate deposits, SPE Reservoir Evaluation and Engineering 10 (2008) 458–488.
551 G. J. Moridis, K. Pruess, User's Manual of the TOUGH+ v1.5 Core Code: A General Purpose Sim-
552 ulator of Non-Isothermal Flow and Transport Through Porous and Fractured Media, Technical
553 Report LBNL-6869E, Lawrence Berkeley National Laboratory, 2014.
554 A. Nishida, Experience in developing an open source scalable software infrastructure in japan, in:
555 Computational Science and Its Applications - ICCSA 2010. Lecture Notes in Computer Science
556 6017.
557 G. J. Moridis, M. B. Kowalsky, K. Pruess, Depressurization-induced gas production from class 1
558 hydrate deposits, SPE Reservoir Evaluation and Engineering 10 (2008) 458–488.
559 G. J. Moridis, M. T. Reagan, Gas production from oceanic class 2 hydrate accumulations, in:
560 Offshore Technology Conference, Houston, Texas.
561 G. J. Moridis, M. T. Reagan, Estimating the upper limit of gas production from class 2 hydrate
562 accumulations in the permafrost, 1: Concepts, system description and the production base case,
563 J. Petr. Sci. Eng. (2010a) 194–201.
564 G. J. Moridis, M. T. Reagan, Estimating the upper limit of gas production from class 2 hydrate
565 accumulations in the permafrost, 2: Alternative well designs and sensitivity analysis, J. Petr.
566 Sci. Eng. 76 (2010b) 124–137.
567 G. J. Moridis, J. Kim, M. T. Reagan, S. j. Kim, Feasibility of gas production from a gas hydrate
568 accumulation at the ubgh2-6 site of the ulleung basin in the korean east sea, Journal of Petroleum
569 Science and Engineering 108 (2013) 180–210.
570 M. T. Reagan, G. J. Moridis, J. N. Johnson, L. Pan, C. M. Freeman, K. L. Boyle, N. D. Keen,
571 J. Husebo, Field-Scale Simulation of Production from Oceanic Gas Hydrate Deposits, Transport
572 In Porous Media, In Press, 2014.
573 G. J. Moridis, M. T. Reagan, Strategies for gas production from oceanic class 3 hydrate accumu-
574 lations, in: Offshore Technology Conference, Houston, Texas.
575 G. J. Moridis, S. Silpngarmlert, M. T. Reagan, T. Collett, K. Zhang, Gas production from a cold,
576 stratigraphically bounded hydrate deposit at the mount elbert site, north slope, alaska, J. Marine
577 Petr. Geol. 28 (2011) 517–534.
578 G. J. Moridis, E. D. Sloan, Gas production potential of disperse low-saturation hydrate accumula-
579 tions in oceanic sediments, J. of Energy Conversion and Management 48 (2007) 1834–1849.
580 G. Li, G. J. Moridis, K. Zhang, X. s. Li, Evaluation of gas production potential from marine gas
581 hydrate deposits in shenhu area of the south china sea, Energy & Fuels 24 (2010) 6018–6033.
582 G. J. Moridis, M. T. Reagan, K. L. Boyle, K. Zhang, Evaluation of the gas production potential
583 of challenging hydrate deposits, Transport in Porous Media 90 (2011) 269–299.
584 G. J. Moridis, User's Manual for the HYDRATE v1.5 option of TOUGH+ v1.5: A Code for the
585 Simulation of System Behavior in Hydrate-Bearing Geologic Media, Technical Report LBNL-
586 6871E, Lawrence Berkeley National Laboratory, 2014.
587 K. Pruess, C. Oldenburg, G. Moridis, TOUGH2 User's Guide, Version 2.0, Technical Report LBNL-
588 43134, Lawrence Berkeley National Laboratory, 1999.
589 K. Pruess, C. Oldenburg, G. Moridis, TOUGH2 User's Guide, Version 2.1, Technical Report LBNL-
590 43134, Lawrence Berkeley National Laboratory, 2012.
591 G. J. Moridis, C. M. Freeman, User's Manual for the REALGASBRINE v1.0 option of TOUGH+:
592 A Code for the Simulation of System Behavior in Gas-Bearing Geologic Media, Technical Report
593 LBNL-6870E, Lawrence Berkeley National Laboratory, 2014.
594 L. J. Klinkenberg, The permeability of porous media to liquids and gases, in: Api Drilling and
595 Production Practice, 1941, pp. 200–213.
596 S. C. Jones, A rapid accurate unsteady-state klinkenberg parameter, SPE Journal (1972) 383–397.
597 Y. Wu, K. Pruess, P. Persoff, Gas flow in porous media with klinkenberg effects, Transp. Porous
598 Media 32 (1988) 117–137.

599 R. J. Millington, J. P. Quirk, Permeability of porous solids, Trans. Faraday Soc. 57 (1961) 1200–
600 1207.
601 R. B. Bird, W. E. Stewart, E. N. Lightfoot, Transport Phenomena, John Wiley & Sons, Inc, New
602 York, 1960.
603 F. A. Florence, J. A. Rushing, K. E. Newsham, T. A. Blasingame, Improved permeability pre-
604 diction relations for low-permeability sands, in: SPE Rocky Mountain Oil and Gas Technology
605 Symposium, Denver, Colorado.
606 C. M. Freeman, G. J. Moridis, T. A. Blasingame, A numerical study of microscale flow behavior
607 in tight gas and shale gas reservoir systems, Transp. in Porous Media 90 (2011) 253–268.
608 G. E. M. Karniadakis, A. Beskok, Micro Flows: Fundamentals and Simulation, Springer, New York,
609 London, 2002.
610 F. Civan, Effective correlation of apparent gas permeability in tight porous media, Transp. in
611 Porous Med 83 (2008) 375–384.
612 P. Forchheimer, Wasserbewewegung durch boden, ZVDI 45 (1901) 1781.
613 R. A. Wattenbarger, H. J. Ramey, Gas well testing with turbulence, damage and wellbore storage,
614 SPE 1835, J. Pet. Tech. (1968) 877–884.
615 D. L. e. a. Katz, Handbook of Natural Gas Engineering, McGraw-Hill, New York, 1959.
616 T. Kneafsey, L. Tomutsa, G. J. Moridis, Y. Seol, B. Freifeld, C. E. Taylor, A. Gupta, Methane
617 hydrate formation and dissociation in partially saturated sand – measurements and observations,
618 in: 5th International Conference on Gas Hydrates, Trondheim, Norway, pp. 213–220.
619 W. Wagner, J. R. Cooper, A. Dittmann, J. Kijima, H. j. Kretzschmar, A. Kruse, R. Mareš,
620 K. Oguchi, H. Sato, I. Stöcker, O. Šifner, Y. Takaishi, I. Tanishita, J. Trübenbach, T. Willkom-
621 men, The iapws industrial formulation 1997 for the thermodynamic properties of water and
622 steam, ASME J. Eng. Gas Turbines and Power 122 (2000) 150–182.
623 International Association for the Properties of Water and Steam (IAPWS), Guideline on a Low-
624 Temperature Extension of the IAPWS-95 Formulation for Water Vapor, Boulder, Colorado, 2012.
625 International Association for the Properties of Water and Steam (IAPWS), Revised Release on the
626 Pressure along the Melting and Sublimation Curves of Ordinary Water Substance, Plzeň, Czech
627 Republic, 2011a.
628 International Association for the Properties of Water and Steam (IAPWS), Release on the IAPWS
629 Formulation 2011 for the Thermal Conductivity of Ordinary Water Substance, Plzeň, Czech
630 Republic, 2011b.
631 International Association for the Properties of Water and Steam (IAPWS), Revised Release on the
632 Equation of State 2006 for H2O Ice Ih, Doorwerth, The Netherlands, 2009.
633 International Association for the Properties of Water and Steam (IAPWS), Release on the IAPWS
634 Formulation 2008 for the Viscosity of Ordinary Water Substance, Berlin, Germany, 2008.
635 International Association for the Properties of Water and Steam (IAPWS), Revised Release on the
636 IAPWS Industrial Formulation 1997 for the Thermodynamic Properties of Water and Steam,
637 Lucerne, Switzerland, 2007.
638 C. Yaws, Chemical Properties Handbook, McGraw-Hill Education, 1999.
639 D. Y. Peng, D. B. Robinson, A new two-constant equation of state, Indust. and Engr. Chemistry:
640 Fundamentals 15 (1976) 59–64.
641 G. Soave, Equilibrium constants from a modified redlich–kwong equation of state, Chem. Eng. Sci.
642 27 (1972) 1197–1203.
643 O. Redlich, J. N. S. Kwong, On the thermodynamics of solutions, Chem. Rev. 44 (1949) 1.
644 B. L. Lee, M. G. Kesler, A generalized thermodynamic correlation based on three-parameter
645 corresponding states, AIChE Journal 21 (1975) 510–527.
646 T. H. Chung, M. Ajlan, L. L. Lee, K. E. Starling, Generalized multiparameter correlation for
647 nonpolar and polar fluid transport properties, Ind. Eng. Chem. Res. 27 (1988) 671–679.
648 S. E. Quiñones-Cisneros, C. K. Zéberg-Mikkelsen, E. H. Stenby, The friction theory (f-theory) for
649 viscosity modeling, Fluid Phase Equilib. 169 (2000) 249–276.

650 E. N. Fuller, K. Ensley, J. C. Giddings, Diffusion of halogenated hydrocarbons in helium: The
651 effect of structure on collision cross sections, J. Phys. Chem. 73 (1969) 3679–3685.
652 M. R. Riazi, C. H. Whitson, Estimating diffusion coefficients of dense fluids, Ind. Eng. Chem. Res.
653 32 (1993) 3081–3088.
654 A. L. Ballard, A Non-Ideal Hydrate Solid Solution Model for a Multi-Phase Equilibria Program,
655 Ph.D. thesis, Colorado School of Mines, 2002.
656 V. A. Kamath, Study of heat transfer characteristics during dissociation of gas hydrates in porous
657 media, Ph.D. thesis, Univ. of Pittsburgh, 1984.
658 G. J. Moridis, M. B. Kowalsky, K. Pruess, tough+hydrate v1.1 User's Manual: A Code for the
659 Simulation of System Behavior in Hydrate-Bearing Geologic Media, Technical Report LBNL-
660 0149E, Lawrence Berkeley National Laboratory, 2009.
661 G. J. Moridis, M. B. Kowalsky, K. Pruess, Tough+hydrate v1.2 User's Manual: A Code for the
662 Simulation of System Behavior in Hydrate-Bearing Geologic Media, Technical Report LBNL-
663 0149E, Lawrence Berkeley National Laboratory, 2012.
664 J. Rutqvist, C. Tsang, A study of caprock hydromechanical changes associated with co2 injection
665 into a brine aquifer, Environmental Geology 42 (2002) 296–305.
666 O. M. Phillips, Flow and Reactions in Permeable Rocks, Cambridge University Press, Cambridge,
667 New York, Melbourne, 1991.
668 H. Pape, C. Clauser, J. Iffland, Permeability prediction based on fractal pore-space geometry,
669 Geophysics 64 (1999) 1447–1460.
670 T. Xu, Y. Ontoy, P. Molling, N. Spycher, M. Parini, K. Pruess, Reactive transport modeling of
671 injection well scaling and acidizing at tiwi field, philippines, Geothermics 33 (2004) 477–491.
672 C. Morrow, D. Lockner, D. Moore, J. Byerlee, Permeability of granite in a temperature gradient,
673 Journal of Geophysical Research 86 (1981) 3002–3008.
674 P. J. Vaughan, Analysis of permeability reduction during flow of heated, aqueous fluid through
675 westerly granite, in: C. F. Tsang (Ed.), Coupled Processes Associated with Nuclear Waste
676 Repositories, Academic Press, New York, 1987, pp. 529–539.
677 A. Verma, K. Pruess, Thermohydrologic conditions and silica redistribution near high-level nuclear
678 wastes emplaced in saturated geological formations, J. of Geophys. Res. 93 (1988) 1159–1173.
679 M. van Genuchten, A closed-form equation for predicting the hydraulic conductivity of unsaturated
680 soils, Soil Sci. Soc. (1980) 892 – 898.
681 A. T. Corey, The interrelation between gas and oil relative permeabilities, Producers Monthly
682 (1954) 38–41.
683 H. L. Stone, Probability model for estimating three-phase relative permeability, Trans. SPE of
684 AIME 249 (1970) 214–218.
685 J. C. Parker, R. J. Lenhard, T. Kuppusamy, A parametric model for constitutive properties gov-
686 erning multiphase flow in porous media, Water Resour. Res. 23 (1987) 618–624.
687 R. H. Brooks, A. T. Corey, Properties of porous media affecting fluid flow, ASCE J. Irrig. Drain
688 Div. 6 (1966) 61.
689 M. C. Leverett, Capillary behavior in porous solids, Trans. Soc. Pet. Eng. AIME 142 (1941)
690 152–169.
691 A. L. Edwards, TRUMP: A Computer Program for Transient and Steady State Temperature Distri-
692 butions in Multidimensional Systems,, Technical Report, National Technical Information Service,
693 National Bureau of Standards, Springfield, VA, 1972.
694 T. N. Narasimhan, P. A. Witherspoon, An integrated finite difference method for analyzing fluid
695 flow in porous media, Water Resour. Res. 12 (1976) 57 – 64.
696 T. N. Narasimhan, P. A. Witherspoon, A. L. Edwards, Numerical model for saturated-unsaturated
697 flow in deformable porous media, part 2: The algorithm, Water Resour. Res. 14 (1978) 255–261.
698 S. Balay, S. Abhyankar, M. F. Adams, J. Brown, P. Brune, K. Buschelman, V. Eijkhout, W. D.
699 Gropp, D. Kaushik, M. G. Knepley, L. C. McInnes, K. Rupp, B. F. Smith, H. Zhang, PETSc
700 Web page, http://www.mcs.anl.gov/petsc, 2014.

701 B. J. Anderson, J. W. Wilder, M. Kurihara, M. D. White, G. J. Moridis, S. J. Wilson, M. Pooladi-
702 Darvish, Y. Masuda, T. S. Collett, R. Hunter, et al., Analysis of modular dynamic formation test
703 results from the mount elbert 01 stratigraphic test well, milne point unit, north slope, alaska,
704 British Columbia, Canada (2008).
705 B. J. Anderson, M. Kurihara, M. D. White, G. J. Moridis, S. J. Wilson, M. Pooladi-Darvish,
706 M. Gaddipati, Y. Masuda, T. S. Collett, R. B. Hunter, et al., Regional long-term production
707 modeling from a single well test, mount elbert gas hydrate stratigraphic test well, alaska north
708 slope, Marine and petroleum geology 28 (2011) 493–501.
709 T. J. Kneafsey, G. J. Moridis, X-ray computed tomography examination and comparison of gas
710 hydrate dissociation in nghp-01 expedition (india) and mount elbert (alaska) sediment cores:
711 Experimental observations and numerical modeling, Marine and Petroleum Geology 58 (2014)
712 526–539.
713 Z. Yin, G. Moridis, H. K. Tan, P. Linga, Numerical analysis of experimental studies of methane
714 hydrate formation in a sandy porous medium, Applied Energy 220 (2018a) 681–704.
715 Z. Yin, G. Moridis, Z. R. Chong, H. K. Tan, P. Linga, Numerical analysis of experimental studies
716 of methane hydrate dissociation induced by depressurization in a sandy porous medium, Applied
717 Energy 230 (2018b) 444–459.
718 M. B. Kowalsky, G. J. Moridis, Comparison of kinetic and equilibrium reactions in simulating the
719 behavior of gas hydrates, Energy Conversion and Management 48 (2007) 1850. (LBNL-63357).